CIRP Annals - Manufacturing Technology 62 (2013) 547–550

Contents lists available at SciVerse ScienceDirect

CIRP Annals - Manufacturing Technology

journal homepage: http://ees.elsevier.com/cirp/default.asp

Correction for lateral distortion in coherence scanning interferometry

Andrew Henning [a], Claudiu Giusca [a], Alistair Forbes [a], Ian Smith [a], Richard Leach (3)[a,*], Jeremy Coupland [b], Rahul Mandal [b]

[a] National Physical Laboratory, Teddington, Middlesex TW11 0LW, UK
[b] Loughborough University, Loughborough, Leicestershire LE11 3TU, UK

Submitted by Chris Evans (1), Charlotte, USA.

ARTICLE INFO

Keywords:
Surface analysis
Measurement
Distortion correction

ABSTRACT

For a complete calibration of optical surface topography measuring instruments, which encompass their ability to measure slope and curvature, a determination of their optical transfer function is required. Errors induced by non-linearity of the scales of the instrument can affect their shift invariant properties, which in turn affect their transfer function. The non-linearity can be caused by distortion produced by the quality of the optical setup. A method to develop a correction model that combines a simple model of optical distortion with error separation techniques is discussed. Experimental tests of the method are presented and measurement uncertainties are investigated.

1. Introduction

Coherence scanning interferometry (CSI) is a versatile three-dimensional (3D) imaging technique which is widely used for the measurement of surface topography [1–3]. CSI is a non-contacting optical method that combines the lateral resolution of a high power optical microscope with the axial resolution of an interferometer and is becoming an increasingly popular alternative to traditional stylus profilers for the measurement of areal surface texture parameters [3]. In essence, CSI exploits broadband, incandescent or LED illumination and a Mirau or Michelson interference objective to record the interference between light reflected from a reference surface and that scattered by the object [2]. Since the source illumination is limited in both temporal and spatial coherence, the interference fringes are observed over a finite scan range and it is relatively straightforward to locate the bright zero order fringe that identifies when path length is balanced in the interferogram.

Despite significant advantages, CSI can exhibit certain problems that restrict its use as a traceable measurement tool in some domains. At present, the causes of measurement error are poorly understood but it is generally accepted that errors are exacerbated by surface tilt [4]. Despite this, CSI instrumentation is usually calibrated axially using step height artefacts and laterally using calibration cross gratings [5], and with this approach, step height measurements have been demonstrated with nanometre-level uncertainty [5]. Recently, a method to calibrate and adjust a CSI instrument has been demonstrated that is based on a determination of the instrument's optical transfer function [6]. This method relies on the assumption that the transfer function is the same throughout the field of view (shift invariance), which implies that there is no lateral distortion of the image. In this paper, it will be shown that commercial CSI instruments can exhibit a significant amount of lateral distortion. This distortion not only affects the lateral capability of the instrument, but if a surface with significant slope is measured, there will also be errors introduced into measurement of heights (and hence surface texture parameters). A method will be described which allows the distortion to be measured and corrected. A commercial CSI instrument was used to obtain the measurement results presented in this paper. The CSI was fitted with a 5× magnification objective lens (in a Michelson configuration, 0.4 numerical aperture, working field of view 0.9 mm by 0.9 mm and sampling distance of approximately 0.88 μm). Note that third order distortion in a Fizeau interferometer produces a tilt dependent height error which typically appears as comatic aberration [7]. The height error can be calibrated and compensated and has been applied to CSI [8]; however, although height errors are corrected in this way, lateral distortion remains.

2. Measurement strategies

In order to assess the distortion in the image gained using the CSI instrument, an artefact with calibrated lateral features is required. The calibration of the artefact, a 17 × 17 array of square pits on a flat surface, is obtained using two separate methods. In the first method, the positions of an array of pits are measured using a traceable areal surface topography measuring instrument, such as the NPL Areal Instrument [9] – a primary contact stylus instrument that measures the motion of the stylus tip using laser interferometers. While the NPL Areal Instrument provides the information that is needed, such a calibration is not widely available and so a second method was also used. In the second method, three images of the object are recorded, with the object being rotated between the first and second images, and with a translation of the object between the second and third images (similar to techniques developed for ball-plate measurement and in lithography [7]). The information contained in these three

* Corresponding author.

0007-8506/$ – see front matter. © 2013 CIRP.
http://dx.doi.org/10.1016/j.cirp.2013.03.026

Table 1
Coefficients of each term in the matrix *C*.

Values in *C*	1	*x*	*y*	x^2	*xy*	y^2	x^3	y^3	x^2y	y^2x
Dewarping x	−0.0006	0.9727	0.0054	−0.0001	0.0001	−0.0000	−0.0020	−0.0004	−0.0001	−0.0017
Linear *x*	−0.0006	0.9715	0.0053	–	–	–	–	–	–	–
Dewarping y	−0.0004	−0.0065	0.9740	−0.0001	0.0001	0.0002	0.0012	−0.0034	−0.0022	0.0001
Linear *y*	−0.0004	−0.0059	0.9720	–	–	–	–	–	–	–

images enables the simultaneous estimation of the systematic errors at the array points and the locations of the features on the artefact, up to a single scale parameter.

The uncertainties associated with these estimates can also be evaluated. With the details of the pits on the artefact obtained, methods to correct distortions in the image can be applied. Three methods for image distortion correction have been considered: a linear correction that corrects for magnification and a more general 'dewarping' algorithm, which corrects for terms including third order (Seidel) distortion and the systematic error corrections generated by the self-calibration method.

2.1. Linear correction and third order dewarping

Once the sets of data points that correspond to the surface of the artefact have been measured by both the traceable instrument and the CSI, a comparison between the sets is made by observing how features (the square pits) are laterally misaligned. Software has been developed to identify these features (protrusions) within the two-dimensional grid of (x, y) values. For each feature, the centroid is calculated. The software returns the distances from the centroid of the pit in the centre of the array, to the centroid of each feature in the grid. An example of the data recorded by the traceable instrument is shown in Fig. 1.

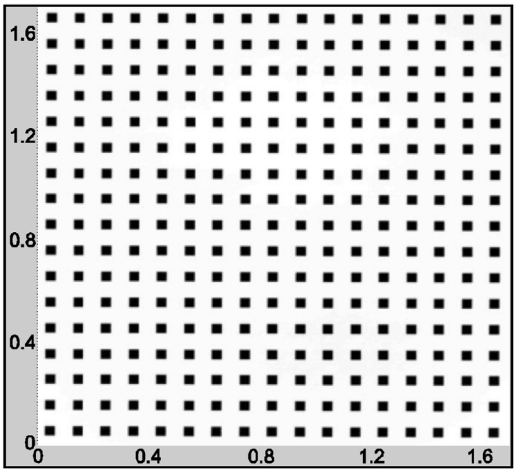

Fig. 1. The height data of the pit array as recorded using the traceable instrument. The axes show the number of the data point in terms of rows and columns measured. The axes are in millimetres.

The dewarping algorithm provides a transformation from the normalised measured (x', y') coordinates in the optically recorded image to the (x, y) coordinates that correspond to the calibrated locations, as given by the traceable instrument (or as gained via the self-calibration method). This transformation is carried out by calculating the location of the centroids in the optical measurement and in the traceable measurement, and matching the former to the latter. In order to do this, an $M \times N$ matrix is constructed, where N is the number of pits in the image and M is the number of terms in the dewarping polynomial. In the case presented here, there are ten terms, those that represent: translations, linear terms, x, y, that represent magnification (and rotation), and higher order terms x^2, xy, y^2, x^3, y^3, xy^2 and x^2y that represent up to third order (Seidel) distortion. Distortions not represented by terms, such as fifth order distortion, will not be compensated; however, the algorithm can be extended to cover further terms if necessary. The coefficients of the polynomial dewarping functions are determined using a least-squares fitting approach. The estimated coefficients can be assembled into a 2×10 matrix, which will be referred to as *C*. The coordinates in one measurement are thus related to those in the other by:

$$x\prime = c_{1,1} + c_{1,2}x + c_{1,3}y + c_{1,4}x^2 + \cdots + c_{1,10}y^2x + \varepsilon_1 \quad (1)$$

$$y\prime = c_{2,1} + c_{2,2}x + c_{2,3}y + c_{2,4}x^2 + \cdots + c_{2,10}y^2x + \varepsilon_2 \quad (2)$$

where ε is an error term, representing the error in the transformation due to distortions that cannot be represented by the limited number of terms in this series. Once *C* has been obtained, it can be used to calculate where on the distorted image the position (x, y) lies. For the desired location, a column vector containing the ten elements: 1, x, y, x^2, xy, y^2, x^3, y^3, x^2y, y^2x is constructed which, when multiplied by *C*, leads to a 2×1 matrix being obtained, where the upper element is the x' location in the distorted image and the lower element y'. The correction can be applied to each pixel, and not just the centroids. By extrapolating the value in the distorted image at each pair (x', y') the corrected image can be generated. Table 1 contains the values for each of the elements of *C* when the dewarping was carried out on the image of the 17×17 array shown in Fig. 1.

The column labelled '1' gives the translation of the origin when calculating the transformation, and each of the other terms is the coefficient for the corresponding element. The dominant elements are in the x and y columns. If there was no distortion, and the two images were not rotated, then the only element in the '*Dewarping x*' row to have any value would be in the 'x' column and would be unity, similarly the only element in '*Dewarping y*' to have any value would be in the 'y' column and again would be unity. While low, the magnitudes of the other terms still have an appreciable effect. Fig. 2 gives the corrected image, that obtained after the dewarping algorithm has been applied, subtracted from the initial image. Here the centroids calculated from the traceable instrument are used as the set of 'true' locations that the dewarping algorithm attempts to correct to. Note that the 'image' from the CSI is actually the average of five images, in order to reduce the effect of noise.

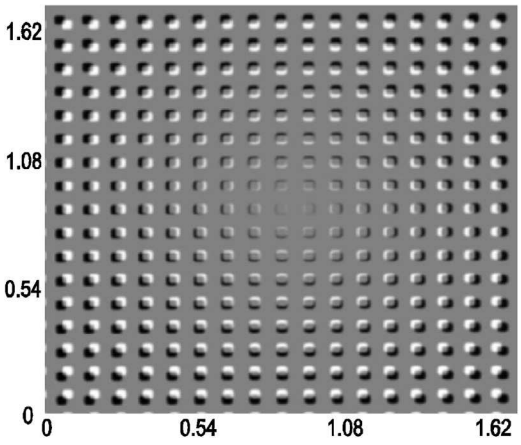

Fig. 2. The image of the pits corrected via dewarping, subtracted from the initial image of the pits. Where the two pits do not completely overlap the area that is covered only by the corrected pit appears black, while that only covered by the uncorrected pits appears white. The axes are in millimetres.

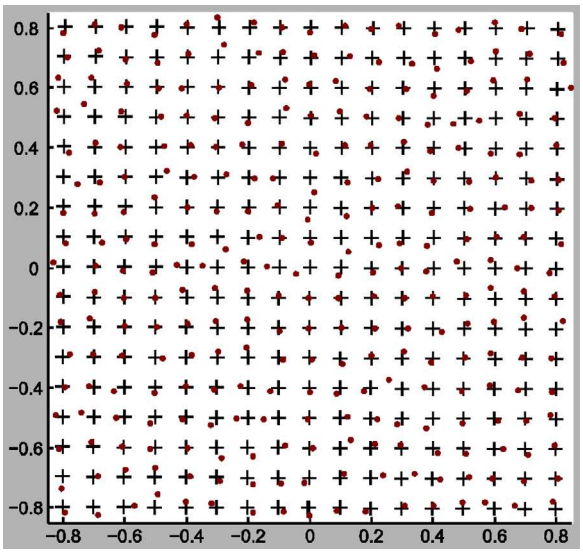

Fig. 3. A plot of the new centroids after dewarping, marked with a '+', and the new centroids plus fifty times the difference between the new centroids and the points given by the traceable instrument, marked with a '·'. The axes are in millimetres.

Fig. 3 shows the locations of the centroids that are calculated from the dewarped image, marked '+' and, in order to show how the errors vary across the image, the new centroids plus fifty times the difference between the centroids after dewarping and the centroids as calculated from the traceable instrument.

The process detailed above is simple to repeat with only corrections that correspond to the translations and terms in x and y. This is achieved by reducing the size of M from ten to three by retaining only the first three terms in the series. The coefficients for each of the terms in C for this case are also shown in Table 1. It can be seen that the values of the coefficients for the first three terms in C for both the dewarping and the linear corrections are very similar. To see where in the image these higher order terms are having an effect, Fig. 4 shows a plot of the difference between the images corrected via dewarping, and via the method only using translations and the linear terms.

To compare the methods, the centroids after the dewarping algorithm, and after the linear correction, are aligned as closely as possible through translation and rotation by a least squares fit, and the greatest distance between the ideal location and the locations after correction are found. Before any correction is applied the greatest distance is 33.59 μm; with a linear correction this is reduced to 1.88 μm, and when corrected with the dewarping algorithm it is 1.10 μm with an associated standard uncertainty

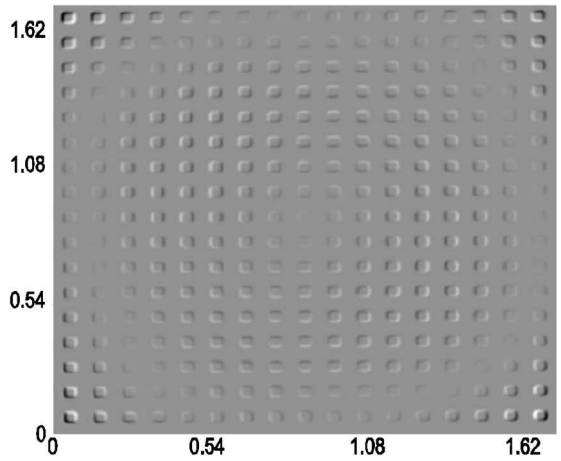

Fig. 4. The image of the pits corrected via dewarping subtracted from the image with a linear correction applied. Where the two pits do not completely overlap the area that is covered only by the positions of the dewarped pit appears black, while that only covered by the linearly corrected pits appears white. Five measurements have been averaged in order to reduce the noise. The axes are in millimetres.

equal to 0.27 μm [10]. The standard measurement uncertainty was dominated by the type A uncertainty associated with both the traceable and CSI measurements. The x and y standard uncertainties of the NPL Areal Instrument do not exceed 8 nm [11]. Often the calibration information of the cross-grating artefacts is limited to the average pitch value and the associated measurement uncertainty. Information about the linearity errors of the pitch is concealed in the measurement uncertainty associated with average pitch value. In such situations, the information carried by the calibration artefact can be inadequate to correct for higher order errors, such as the distortion effect of optical systems, hence, the need to use an error separation technique that allows compensation for linearity errors described by higher order polynomials. Furthermore, the scale information that is necessary for traceability is not essential for the correction of distortion.

2.2. Reference points by self-calibration

While the process up until now has required information from a calibrated artefact, the following method does not rely on this information – it is a self-calibration technique [8,12]. In this method, three images are taken of the array of pits, with the second of the images being of the object after a rotation, and the third image being the object in the second image translated in the x direction by the distance between two rows of points. To reduce noise an average of five images in each position are taken.

In addition scale information must be provided, with all the results being scaled by this factor. Here the scale is obtained by comparison of the corrected centroids to those given by the traceable measurements. In general, an estimate of the distance between any two points on the artefact would suffice. To obtain this estimate of the scale, a summation of the distance from the central pit to each of the other pits is made for both the traceable measurement and the corrected optical measurement, and the ratio of these two summations is used. The uncertainty contribution for this scale correction can be derived from the uncertainty budget for the NPL Areal Instrument.

Fig. 5 shows a plot of the centroids obtained optically, marked by '+', and the points plus twenty times the correction from the observed location towards the 'true' location. The twenty times multiplication is included to show how the corrections vary. It can be seen that the distortion is not the same across the object as the points observed optically on the left hand side are further out in the y direction than the 'true' points, while on the right hand side they are too close to the origin. In addition to calculating the correct

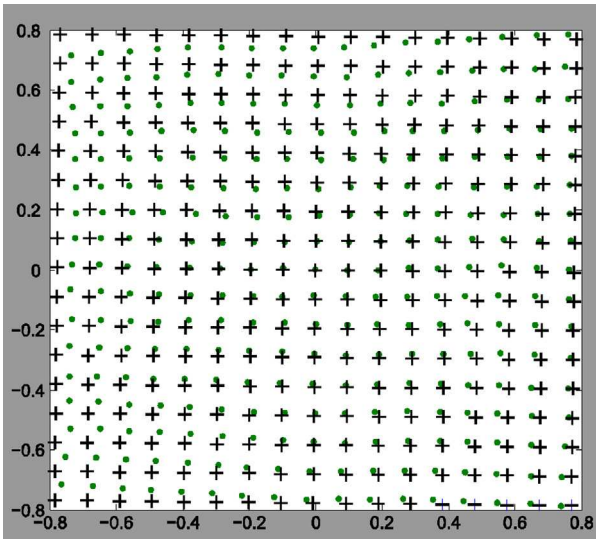

Fig. 5. Plot of the observed centroids of the pits, marked with crosses, and an exaggerated correction to demonstrate how the distortion varies across the image. The points correspond to the observed point plus twenty times the correction shift. It can be seen that the errors on the left and right hand sides lie at different sides of the apparent points. Axes are in millimetres.

Table 2
The elements of *C* used in Section 2.2.

Values in *C*	1	*x*	*y*	x^2	*xy*	y^2	x^3	y^3	x^2y	y^2x
Dewarping *x*	0.0000	0.9984	0.0005	0.0011	0.0003	−0.0011	−0.0008	−0.0010	0.0001	0.0003
Dewarping *y*	0.0000	0.0002	0.9973	0.0008	0.0021	−0.0010	−0.0003	0.0017	−0.0002	0.0003

positions, the self-calibration method can be used to calculate uncertainties in the size and shape for each centroid. In Fig. 5, the maximum uncertainty in size and shape errors for the centroid is 0.70 μm.

To examine how the limited number of terms in the dewarping algorithm affects its ability to compensate for distortions, a comparison between the corrections given by the self-calibration method and the dewarping algorithm is made. To do this the initial image used in the self-calibration method (that taken before the rotation and translations) is used in both methods as the starting point. The corrected centroids given by the self-calibration method are used as the targets that the dewarping algorithm tries to match.

The values in this new *C* matrix are shown in Table 2. If the distortions included in the dewarping algorithm can represent the shifts given by the self-calibration method, then the shift of the two methods will be the same. A least squares method is again used to minimise the difference between the grids given by the self-calibration method and the dewarping algorithm before the maximum error is stated. The maximum difference between the initial position of the centroids and those points where the 'true' position lies is 33.71 μm, as given by this method. The maximum difference between the corrected points given by the dewarping algorithm and the 'true' locations is 1.49 μm. While this shows that the corrections are not equivalent, the vast majority of the correction is captured by the use of the dewarping algorithm. The advantage of the error separation approach is that it does not depend on a particular choice of model, linear, quadratic, etc., to describe the error behaviour. Instead, the systematic effects at the grid points are estimated directly. The disadvantage of the approach is that only errors at the grid points are estimated and errors at other locations have to be estimated using an interpolation scheme. Fitting the dewarping model to the estimated systematic errors is one approach. Other interpolation approaches based on spatially correlated models are being investigated.

3. Conclusions

Several different ways of correcting for the distortion errors found in optical instruments have been compared. While linear corrections are simple to calculate and apply, comparisons of the corrected results with data from the NPL Areal Instrument show that there are still significant errors that are not being corrected for; these errors being most significant in the corners of the image (as expected). The dewarping captures more complex distortions, and in the case that has been considered here, after corrections the results show reasonable improvement over the linear corrections. The method is simple and quick to apply, and if an artefact that fills the field of view is used then the coefficients that are calculated to correct the image may be applied to any object in the field of view, providing improvements to measurements without the need for another calibrated object. The dewarping algorithm does have limitations in the form of the errors that it can correct for, although extending the order of the corrections that are captured by this method is trivial (but will push up the computational requirements accordingly).

The error separation and self-calibration method provides a method that is not limited to corrections below third order, and for which the calculation of errors has been previously considered. While this method is more complex to apply, the results that are obtained give far more detailed views of the errors that are associated with the measurement, separating out the errors due to the machine and the measurements along with variances associated with the parameters. When the same measured information and solution is entered into the dewarping algorithm it may be seen that the corrections are smaller.

Further work will be carried out to verify this work using a second calibrated object; the corrections determined for the initial object should be shown to correct the second as well. Further work will also be carried out to assess the uncertainties in the corrections. As this work has been carried out only on one microscope, these methods will be applied to other machines in future to allow us to gauge the general need for higher order corrections.

Acknowledgement

This work was funded by the NMS Engineering & Flow Metrology Programme 2011–2014.

References

[1] Lee BS, Strand TC (1990) Profilometry with a Coherence Scanning Microscope. *Applied Optics* 29:3784–3788.
[2] Deck L, de Groot P (1994) High-Speed Noncontact Profiler Based on Scanning White-Light Interferometry. *Applied Optics* 33:7334–7338.
[3] Leach RK (2011) *Optical Measurement of Surface Topography*, Springer, Berlin.
[4] Gao F, Leach RK, Petzing J, Coupland JM (2008) Surface Measurement Errors Using Commercial Scanning White Light Interferometers. *Measurement Science and Technology* 19:015303.
[5] Giusca CL, Leach RK, Helary F (2012) Calibration of the Scales of Areal Surface Topography-Measuring Instruments: Part 2. Amplification, Linearity and Squareness. *Measurement Science and Technology* 23:065005.
[6] Mandal R, Padodhi K, Coupland JM, Leach RK (2012) Application of Linear Systems Theory to Characterise Coherence Scanning Interferometry. *Proceedings of SPIE* 8430T.
[7] Evans CJ, Hocken RJ, Estler WT (1993) Self-Calibration: Reversal, Redundancy, Error Separation and 'Absolute Testing'. *Annals of CIRP* 45:617–634.
[8] Deck LL, Evans CJ (2005) High Performance Fizeau and Scanning White-Light Interferometers for Mid-Spatial Frequency Testing of Free-Form Optics. *Proceedings of SPIE* 5921:73–80.
[9] Leach RK, Giusca CL, Naoi K (2009) Development an Characterisation of a New Instrument for the Traceable Measurement of Areal Surface Texture. *Measurement Science and Technology* 20:125102.
[10] BIPM, IEC, IFCC, ISO, IUPAC, IUPAP, OI ML (2008) Guide to the Expression of Uncertainty in Measurement, (Bureau International des Poids et Mesures). *JCGM* 100.
[11] Giusca CL, Leach RK, Forbes AB (2011) A Virtual Machine-Based Uncertainty Evaluation for a Traceable Areal Surface Texture Measuring Instrument. *Measurement* 44:988–993.
[12] Downs MJ, Forbes AB, Siddle JE (1998) The Verification of a High-Precision Two-Dimensional Measurement System. *Measurement Science and Technology* 9:1111–1114.